# The Role of Fluid Turbulence on Contact Electrification of Suspended Particles

Xing Jin and Jeffrey S. Marshall School of Engineering, The University of Vermont

<u>Corresponding Author</u>: Jeffrey S. Marshall, School of Engineering, The University of Vermont, Burlington, VT 05405, U.S.A. PHONE: 1 (802) 656-3826, EMAIL: jmarshal@uvm.edu.

<u>Keywords</u>: contact electrification; turbulence; particle collision; Stokes number

#### Abstract

A probabilistic version of a well-known phenomenological model for contact electrification is used to examine the effect of fluid turbulence on charge development for suspended particles as a function of the particle Stokes number. The distribution of particle collisions and particle charge appear to approach asymptotic states for high values of the Kolmogorov-scale Stokes numbers, exhibiting approximately normal distributions. The influence on particle contact electrification of differences in initial charge carrier density and in particle size are examined.

#### 1. Introduction

Contact electrification is the transfer of charge that occurs when two particles collide with each other or when a particle collides with or rolls along a surface (Marshall and Li, 2014). This phenomenon of charge transfer is usually called *contact electrification* when it occurs as a result of particle collisions and it is called *triboelectric charging* (or tribocharging) when it occurs due to frictional contact between materials that slide or roll relative to each other. Contact electrification of particulates in a turbulent flow occurs widely in both industrial and natural processes. Contact electrification in various process industries, such as coal mining, sawmills, grain mills and storage facilities, is known to lead to dangerous explosions of dust clouds (Eckhoff, 1997). Contact electrification is responsible for development of electric field gradients leading to formation of lightning in sandstorms (Latham, 1964; Williams et al., 2009; Zheng, 2013) and volcanic eruptions (Brook et al., 1974; Tomas, 2007). Contact electrification due to dust storms plays a particularly important role on dusty planets, such as Mars, where it is responsible for the strong ambient charging of dust particles (Eden, 1973; Forward et al., 2009; Harrison et al., 2016). A leading theory for development of electric charge within thunderstorms is that it is caused by contact electrification due to collision of ice particles within the storm cell (Saunders, 1994; Helsdon et al., 2001). Similarly, contact electrification of ice particles in planetary ring systems, such as that of Saturn, lead to particle charging that influences the structure of the rings and their interaction with the planetary atmosphere (Hartquist et al., 2003; Kempf et al., 2006). A theoretical study by Desch and Cuzzi (2000) propose contact electrification of micrometer-scale particles in a turbulent environment as being responsible for formation of lightning in the solar nebula, which is important for formation of the small mmscale chondrules that serve as the building blocks of the planetary system.

There has been a great deal of recent research on fundamental issues associated with particle contact electrification. Despite its importance to a large range of problems, many fundamental aspects of contact electrification remain unresolved. Even the most basic question of what exactly is transferred between the two colliding materials that gives rise to the charge differential is at present not entirely clear, and may in fact differ for different types of contact electrification processes. The problem is not a lack of explanations for the electrification process, but instead too many plausible explanations. Material particles, ions and electrons have all been proposed as possible charge carriers (Williams, 2012; Baytekin et al., 2012; McCarty and Whitesides, 2008; Lacks and Sankaran, 2011; Waitukaitis et al., 2014). A traditional view of contact electrification is represented by the triboelectric series, which empirically orders materials to indicate the direction of charge transfer during contact electrification. However, the triboelectric series is not always reproducible (Lowell and Rose-Innes, 1980; Harper, 1998), and order within the series can sometimes be reversed, such as following ultraviolet irradiation (Kittaka, 1979). Contact electrification has also frequently been observed between chemically identical insulator particles (Lowell et al., 1986; Kok and Lacks, 2009; Siu et al., 2014). Material inhomogeneity, asymmetric contact, electron band gap defects, and local polarization have all been used to explain the charging mechanism (Baytekin et al., 2011; Lacks and Levandovsky, 2007; Lacks and Sankaran, 2011; Pähtz et al., 2007; Lowell and Truscott, 1986).

Despite on-going research on the fundamental physics of contact electrification, reasonable phenomenological models of particle charge exchange exist with which one might proceed to investigate other issues associated with the phenomenon (Duff and Lacks, 2008; Kok and Lacks, 2009; Xie et al., 2013; Apodaca et al., 2010). Following this line of thought, the current paper examines the influence of the surrounding turbulent flow field on the particle

electrification process. We note that contact electrification examples, such as those discussed in the first paragraph of this section, take place in a wide variety of fluid flow environments, ranging from normal earth atmosphere to the low-pressure Martian atmosphere to the nearvacuum conditions of Saturn's rings, and for particle sizes ranging from about 1 μm to 1 cm. The degree of interaction between the colliding particles and the fluid in which they are suspended can be characterized by a dimensionless parameter called the Stokes number, St, which is defined as the ratio of the characteristic time scale  $\tau_p$  for particle drift relative to the fluid and the fluid time scale  $\tau_f$ . For sufficiently small particles the Stokes drag law can be used to write the particle time scale as  $\tau_p = m/3\pi\mu d$ , where m and d are the particle mass and diameter, respectively, and  $\mu$  is the fluid viscosity. The fluid time scale is typically taken to be the fluid convective time, given by the ratio  $\tau_f = L/U$  of the characteristic fluid length scale L to the fluid velocity scale U. For small values of St, the particles are in an orthokinetic regime in which they move with the local fluid velocity and the collisions between particles are primarily due to the local fluid shear flow (Saffman and Turner, 1965). For values of St close to unity, the particles are in an accelerative-correlated regime and particles will drift considerably relative to the fluid. For heavy particles at sufficiently high concentration in a turbulent fluid, the drift induced by centrifugal force causes particles to cluster in high-concentration sheets lying inbetween the turbulent eddy structures (Squires and Eaton, 1991; Bec et al., 2007; Grits et al., 2006; Falkovich and Pumir, 2004). For St much larger than unity, the particles are in an accelerative-independent regime in which particle inertia is sufficiently large that particle motion is only slightly influenced by the fluid forces (Abrahamson, 1975).

The current paper utilizes a probabilistic contact electrification model, together with a hard-sphere discrete element method for particle collisions and a pseudo-spectral method for

direct numerical simulation of homogeneous turbulence, to examine the effect of the background turbulence on contact electrification of the particles for different Stokes numbers. Both the effect of turbulent flow on the overall rate of contact electrification and on the collision and charge distribution are examined. The computational models used in the research are summarized in Section 2. Results of the paper are presented and discussed in Section 3, including the effect of Stokes number on contact electrification and an examination of contact electrification with bidisperse mixtures of particle size and initial charge carrier density. Conclusions are given in Section 4.

## 2. Computational Methods

# 2.1. Particle transport

The particle collisions were simulated using the hard-sphere model, as described by Crowe et al. (1998). The hard-sphere model solves the particle impulse equations during collisions to obtain the post-collision particle velocities  $\mathbf{v}_n(i+1)$  from the given pre-collision velocities  $\mathbf{v}_n(i)$  and restitution coefficient e. For two particles labeled 1 and 2, the restitution coefficient is defined by

$$e_{rest} = \frac{\left[ \mathbf{v}_1(i+1) - \mathbf{v}_2(i+1) \right] \cdot \mathbf{n} |}{\left[ \mathbf{v}_1(i) - \mathbf{v}_2(i) \right] \cdot \mathbf{n} |},$$
(1)

where  $\mathbf{n}$  is the unit normal vector from the centroid of particle 1 to that of particle 2. The hardsphere model also solves the angular impulse equations to obtain the particle angular rotation rate after the collision. The model uses Coulomb's law of friction for the sliding force and assumes that once a particle stops sliding, there is no later sliding of the particle. During the time period in-between collisions, the simulation method solves the particle momentum and angular momentum equations for the particle velocity and rotation rate, subject to forces and torques induced by the fluid, including viscous drag and torque, Saffman lift (Saffman, 1965, 1968), and Magnus lift (Rubinow and Keller, 1961). Added mass force, pressure gradient force and Bassett force are negligible based on the parameter values used in the computations. Electrostatic forces (Coulomb and dielectrophoretic forces) were also neglected on the assumption that particle charges were too weak for these forces to be significant in comparison to the fluid drag. The fluid velocity was interpolated from a 128<sup>3</sup> Cartesian grid onto the particle locations with cubic accuracy using the M4' variation of the B-spline interpolation method developed by Monaghan (1985).

As two particles collide, the contact force between the particles is transmitted via a flattened contact region, across which the particle surfaces are separated by a small gap of width  $\delta$ . The gap thickness is on the order of a nanometer, which for micrometer-scale or larger particles is much less than the particle diameter. For spherical particles, the contact region has a circular shape with radius a(t). For non-adhesive particles, the contact region radius starts at a value of zero at the onset of contact, increases during the compression stage of the collision to a maximum value of  $a_{\rm max}$ , and then decreases again during the recovery stage of the collision until it vanishes again at the particle detachment point. An expression for the maximum contact region radius can be obtained using the Hertz contact theory as (Hertz, 1882; see also Marshall and Li, 2014)

$$a_{\text{max}} = \left(\frac{15Mw_r^2 R^2}{16E}\right)^{1/5},\tag{2}$$

where  $w_r = |[\mathbf{v}_2(i) - \mathbf{v}_1(i)] \cdot \mathbf{n}|$  is the relative radial velocity between two particles labeled '1' and '2' prior to the  $i^{\text{th}}$  collision, and M, R and E are the effective mass, radius and elastic coefficient of the colliding particle pair, defined by

$$\frac{1}{M} \equiv \frac{1}{m_1} + \frac{1}{m_2}, \qquad \frac{1}{R} \equiv \frac{1}{r_1} + \frac{1}{r_2}, \qquad \frac{1}{E} \equiv \frac{1 - v_1^2}{E_1} + \frac{1 - v_2^2}{E_2}. \tag{3}$$

Here  $m_n$ ,  $r_n$ ,  $E_n$ , and  $v_n$  denote the mass, radius, elastic modulus and Poisson's ratio for particle n, respectively.

### 2.2. Contact electrification

The phenomenological contact electrification model used in the current study is a stochastic version of the model proposed by Duff and Lacks (2008) and Lacks and Levandovsky (2007). The original model assumed that the charge carrier for contact electrification is a set of electrons trapped in high-energy band gaps, which transfer into a low-energy state when transported to a second particle during particle collision. However, it was noted by Castle (2008) that the model is equally valid with ions as the charge carrier (see also Waitukaitis et al., 2014). The number of charge carriers at time t is denoted by  $N_{H,n}(t)$  on a particle n with diameter  $d_n$ . If the initial surface number density of charge carriers is  $\rho_n$ , then  $N_{H,n}(0) = \pi d_n^2 \rho_n$ . When a particle collides with another particle, each particle transfers to the other particle all of the charge

carriers within a distance  $r_{cut}$  of the contact point, where the contact point is the centroid of the contact region. For instance, in a collision between particles 1 and 2 at a time  $t_c$  in which charge carriers are exchanged between both particles, the change in number of charge carriers,  $N_{H,n}(t)$ , for each particle is given by

$$\Delta N_{H,1} = -\pi r_{cut}^2 \rho_1, \qquad \Delta N_{H,2} = -\pi r_{cut}^2 \rho_2.$$
 (4)

The change in particle charge due to the collision is given simply by the product of the number of charge carriers exchanged and the electric charge  $e_{\rm C}$  per charge carrier. Duff and Lacks (2008) examined several different values for the distance  $r_{\rm cut}$  and found that the value selected did not significantly modify the qualitative nature of the contact electrification predictions. Since typical charge carriers, such as high-energy electrons or ions, can only travel short distances either between particles or on a particle surface, the physically correct value of  $r_{\rm cut}$  is the maximum contact region radius  $a_{\rm max}$ , given by (2). However, this choice can lead to a requirement for a large number of computations per particle in order to observe significant contact electrification, and so might not be computationally feasible. A reasonable approach to accelerate the numerical computation is to prescribe  $r_{\rm cut}$  to a be a multiple of  $a_{\rm max}$ , such that

$$r_{cut} = Da_{\max}, \tag{5}$$

where  $D \ge 1$  is an acceleration factor.

At any time t, the surface of a particle consists of some regions with available charge carriers and some regions in which the charge carriers have already been cleared away by transfer to another particle. If particle 1 collides with a second particle 2 in a contact region with available charge carriers on particle 1 but without available charge carriers on particle 2, then the electric charge is transferred only from particle 1 to particle 2, but not from particle 2 to particle 1. Duff and Lacks (2008) presented a computational approach in which they used a set of subparticles attached to the particle surfaces to represent high-energy electrons on the surface, which were then removed within a region of radius  $r_{cut}$  following each collision. Of course, this approach is quite time-consuming for large numbers of particles. In the current paper, we alternatively propose a stochastic approach for dealing with depletion of charge carriers from the particle surface. Specifically, we denote by  $A_{H,n}(t)$  the total area on a particle n with available charge carriers at time t, such that at the initial time  $A_{H,n}(0) = A_n \equiv \pi d_n^2$ , where  $A_n$  is the surface area of particle n. A collision of particle 1 with another particle 2 is considered to consist of two stages – a forward transfer of charge carriers from particle 1 to particle 2 and a reverse transfer from particle 2 to particle 1. In the forward transfer stage, we select a random variable  $p_1$  with uniform probability distribution between 0 and 1. If  $p_1 \le A_{H,1}(t)/A_1$ , then the collision is taken to have occurred at a location with available charge carriers on particle 1. In this case, the change in number of charge carriers and the change in area occupied by available charge carriers on particle 1 are given by

$$\Delta N_{H,1} = -\pi r_{cut}^2 \rho_1, \qquad \Delta A_{H,1} = -\pi r_{cut}^2.$$
 (6)

If  $p_1 > A_{H,1}(t)/A_1$ , then the collision is taken to have occurred at a location with no available charge carriers on particle 1, and there is no change in the number of charge carriers or in  $A_{H,1}$ . In the reverse transfer stage, we again select a random number  $p_2$  with the same probability distribution. If  $p_2 \le A_{H,2}(t)/A_2$ , then the collision is taken to have occurred at a location with available charge carriers on particle 2, such that

$$\Delta N_{H,2} = -\pi r_{cut}^2 \rho_2, \qquad \Delta A_{H,2} = -\pi r_{cut}^2.$$
 (7)

Again, no changes are made if  $p_2 > A_{H,2}(t)/A_2$ . After both the forward and reverse transfer stages of contact electrification are completed, the net change in charge of the two particles over the time step is given by

$$\Delta Q_1 = -\Delta Q_2 = e_C \left( \Delta N_{H,1} - \Delta N_{H,2} \right). \tag{8}$$

#### 2.3. Fluid flow

The direct numerical simulations (DNS) of isotropic, homogeneous turbulence used to represent a turbulent fluid flow were performed using a triply-periodic pseudo-spectral method with second-order Adams-Bashforth time stepping and exact integration of the viscous term (Vincent and Meneguzzi, 1991). The spectral Navier-Stokes equations were evolved in time after having been projected onto a divergence-free space using the operator  $P_{ij} = k_i k_j / k^2 - \delta_{ij}$  according to the expression

$$\overline{\mathbf{u}}^{n+1} = \overline{\mathbf{u}}^n \exp(-\nu k^2 \Delta t) + \Delta t \, \mathbf{P} \cdot \left[ \frac{3}{2} \overline{\mathbf{F}}^n \exp(-\nu k^2 \Delta t) - \frac{1}{2} \overline{\mathbf{F}}^{n-1} \exp(-2\nu k^2 \Delta t) \right], \tag{9}$$

where an overbar denotes Fourier transform in three space dimensions, a superscript indicates the time step, and  $\mathbf{k}$  is the wavenumber vector with magnitude k. The force vector  $\mathbf{F}$  on the right-hand side has Fourier transform given by

$$\overline{\mathbf{F}} = \overline{\mathbf{u} \times \mathbf{\omega}} + \overline{\mathbf{f}}_{F} \,, \tag{10}$$

where  $\bar{\mathbf{f}}_F$  is the small wavenumber forcing term required to maintain the turbulence with approximately constant kinetic energy. The velocity field was made divergence-free at each time step by taking its Fourier transform and using the spectral form of the continuity equation, given by

$$\mathbf{k} \cdot \overline{\mathbf{u}} = 0. \tag{11}$$

The forcing vector was assumed to be proportional to the fluid velocity (Lundgren, 2003; Rosales and Meneveau, 2005), such that

$$\bar{\mathbf{f}}_{F} = \left\{ \begin{array}{ll} C\overline{\mathbf{u}} & \text{for } k < k_{crit} \\ 0 & \text{for } k > k_{crit} \end{array} \right. \tag{12}$$

where the coefficient C was adjusted at each time step so as to maintain approximately constant turbulent kinetic energy. The current computations were performed with  $k_{crit} = 5$ , so that the forcing acts only on the large-scale eddies.

The fluid flow computations were performed on a  $128^3$  cubic grid with domain side length  $2\pi$ . A preliminary computation was conducted with no particles to allow the turbulence to develop a range of length scales characteristic of statistically stationary homogeneous isotropic turbulence for 5000 time steps with a time step size of  $\Delta t = 0.005$ . The computation was then restarted with 64,000 particles randomly distributed in the computational domain and with the initial particle velocity set equal to the local fluid velocity. The turbulence kinetic energy q and dissipation rate  $\varepsilon$  were obtained from integration of the power spectrum, e(k), as

$$q = \int_0^{k_{\text{max}}} e(k)dk, \qquad \varepsilon = 2\nu \int_0^{k_{\text{max}}} k^2 e(k)dk. \qquad (13)$$

Various dimensionless measures describing the turbulence in the validation computations are listed in Table 1, including the root-mean-square velocity magnitude  $u_0$ , the average turbulence kinetic energy q, the integral length scale  $\ell_0 = 0.5 \, u_0^{-3} / \varepsilon$ , the Taylor microscale  $\lambda = (15 \nu / \varepsilon)^{1/2} u_0$ , and the Kolmogorov length scale  $\eta = (\nu^3 / \varepsilon)^{1/4}$ . The corresponding microscale Reynolds number is  $\mathrm{Re}_{\lambda} = u_0 \lambda / \nu = 99$ .

## 3. Results for Particle Contact Electrification

## 3.1. Characteristics of the turbulent flow

The direct numerical simulations (DNS) of the turbulent flow field were conducted assuming one-way coupling with the particles. The computed power spectrum e(k) is plotted in Figure 1a as a function of the product of the wavenumber magnitude k and the Kolmogorov length scale  $\eta = (v^3/\varepsilon)^{1/4}$ , showing the expected  $k^{-5/3}$  dependence in the inertial range and a faster drop-off for higher wavenumber in the dissipation range. The computed velocity probability density function (p.d.f.) in one coordinate direction (x-direction), normalized by the root-mean-square velocity, is shown in Figure 1b. The DNS predictions are observed to be close to a best-fit Gaussian curve  $p(v) = 0.8 \exp(-0.5v^2)$ , where  $v \equiv v_x / v_{x,rms}$ , in agreement with standard observations for the turbulence flows (Voth et al., 1998). The p.d.f. of the x-component of the fluctuating fluid acceleration field is plotted in Figure 1c. Fluid acceleration is computed from the DNS velocity field for post-processing purposes using a centered difference approximation in space and a forward difference in time. Also shown in this figure is the empirical expression for the p.d.f.,

$$p(a) = 1.8 \exp\left[-a^2/\{(1+\left|ac_1/c_2\right|^{c_3})c_2^2\}\right], \tag{14}$$

obtained experimentally by La Porta et al. (2001). In this expression,  $a \equiv a_x/a_{x,rms}$ , and the coefficients are given by a best fit to La Porta et al.'s experimental data as  $c_1 = 0.539$ ,  $c_2 = 0.508$ , and  $c_3 = 1.588$ . The acceleration p.d.f. exhibits a non-Gaussian "superstatistical" distribution characterized by a fat tail, which is typical of a highly intermittent signal (Beck, 2008; Biferale et al., 2004; Reynolds, 2003). Mordant et al. (2004) suggested that the observed

acceleration intermittency in turbulent flows can be associated with the presence of coherent vortex structures.

#### 3.2. Effect of Stokes number on contact electrification

The effect of fluid flow on the particle collision and electrification was examined by conducting a series of simulations with different values of the Kolmogorov-scale Stokes number, St, defined by

$$St = \frac{\tau_P}{\tau_K}. \tag{15}$$

Here, the particle time scale  $\tau_p = m/3\pi d\mu$  is a function of the particle mass m and diameter d and the fluid viscosity  $\mu$ , and the Kolmogorov time scale is defined by  $\tau_K = (v/\varepsilon)^{1/2}$ . Computations were performed for a set of six Stokes numbers ranging from 1.1 to 33.6. In all computations, the total number collisions in the system B(t) exhibits approximately linear increase with time after a short transient period. The slope of B(t) following the initial transient, divided by the computational volume  $(2\pi)^3$ , yields the collision rate per unit volume,  $\dot{n}_c$ . We plot the variation of  $\dot{n}_c$  with the Stokes number in Figure 2. The collision rate exhibits a peak near St = 5. A comparison of our predicted collision rates with those obtained from previous studies of particle collision in homogeneous isotropic turbulence is shown in Figure 3, in which we plot the dimensionless ratio  $\dot{n}_c/(\pi d^2 n_p^2 u_0)$  predicted in the current study (at  $Re_\lambda = 99$ ) with values reported by Sundaram and Collins (1997) for  $Re_\lambda = 54.2$ , Wang et al. (2000) for

 $Re_{\lambda} = 75$ , and Fayed and Ragab (2013) for  $Re_{\lambda} = 96$ . Here,  $n_p$  is the particle number density. The predicted value of this dimensionless collision rate obtained in the current computations is observed to have a similar range of values as those obtained from these other three studies.

For small values of Stokes number (St  $\leq$  0.4), the local fluid flow can push two particles together to generate a *chattering* type of collision, resulting in rapid repeated collisions as the particles cyclically push apart under their elastic rebound force and are then driven together again by the fluid forces. As discussed by Sundaram and Collins (1996), these repeated collisions would in reality be modulated by vortices shed from the particles, which are not included in the current particle force modeling based on the one-way coupling assumption. We have therefore considered only Stokes number values that are sufficiently large that this chattering type of collision does not occur.

The approach of the particle system to an equilibrium charge state can be observed by plotting the time variation of the total transferred charge,  $Q_{trans}$ , defined as half of the sum of the absolute value of the charge of each particle. The total transferred charge is plotted in Figure 4 as a function of time for different Stokes numbers. The value of  $Q_{trans}$  approaches an equilibrium value at long time, after all the charge carriers initially attached to the particles in the system have been expended via collisions with other particles in the system. The larger the collision rate  $\dot{n}_c$ , the more opportunities for a particle to transfer charge, and hence the more quickly this equilibrium condition is attained. However, the results in Figure 4 also depend on the relative velocity at collision between the particles, which effects the contact area as indicated in (2) and hence the number of charge carriers that are transferred at each collision. For Stokes numbers above about 6, the differences in value of  $\dot{n}_c$  in Figure 2 and in the plot of  $Q_{trans}$  versus time in Figure 4 are observed to be small.

For a closer examination of particle collision, we count the number of collisions for each particle, denoted by  $b_p$ , and compute the probability density function (p.d.f.) of collision number by dividing the range of variation of  $b_p$  into equal-size bins. The resulting p.d.f. for collision number is plotted in Figure 5 for St = 33.6 at five different values of the total number of collisions in the system, B. The p.d.f. of collision number at this Stokes number is observed to closely approximate a normal distribution, as indicated by the curves plotted in Figure 5. As run time increases and the total number of collisions in the system accumulates, the distribution of number of collisions grows wider. To facilitate a comparison of different Stokes number cases, the collision number p.d.f. is plotted in Figure 6 by dividing the value of  $b_p$  by the total number of collisions B, and also by multiplying the value of the y-axis variable by B to ensure that the integral of the p.d.f. is equal to unity. The plot in Figure 6 is made for different Stokes number values at a time when the total number of collisions is B = 500,000. The resulting p.d.f. plot approaches a common normal distribution as the value of Stokes number increases, with mean value  $\langle b_p/B \rangle = 3.1 \times 10^{-5}$ .

The observation that the collision distribution approaches a normally-distributed p.d.f. can be explained with use of the central limit theorem. For each collision, the probability that a given particle i is involved in this collision is

$$p = \frac{N_p - 1}{N_p (N_p - 1)/2} = \frac{2}{N_p},$$
(16)

where  $N_p$  is the total number of particles in the computational system. Assuming linear variation in time t, the total number of collisions B can be written as  $B = \dot{n}_c V t$ , where V is the volume of the computational domain. After B collisions in the system, the probability of particle i having undergone s collisions can be expressed as

$$P(s,B) = \binom{B}{s} p^{s} (1-p)^{B-s}, \tag{17}$$

which is a binomial distribution with mean  $\mu = Bp$  and variance  $\sigma^2 = Bp(1-p)$ , where p is a constant given by (16). When B becomes large, Stirling's approximation  $B! \sim B^B e^{-B} \sqrt{2\pi B}$  can be used to yield an asymptotic approximation for (17) as

$$P(s,B) \sim (\frac{Bp}{s})^s (\frac{B(1-p)}{B-s})^{B-s} \sqrt{\frac{B}{2\pi s(B-s)}}$$
 (18)

Under the further assumption that  $\left|\frac{s}{pB}-1\right|<<1$ , the term  $(\frac{Bp}{s})^s(\frac{B(1-p)}{B-s})^{B-s}$  in (18) can be approximated as  $e^{-(s-Bp)^2/2Bp(1-p)}$  with use of the Taylor series expansion for  $\ln(1+x)=x-\frac{1}{2}x^2+\mathrm{O}(x^3)$ , so that (18) becomes

$$P(s,B) \sim \sqrt{\frac{1}{2\pi Bp(1-p)}} e^{-(s-Bp)^2/2Bp(1-p)} = \frac{1}{\sqrt{2\pi\sigma^2}} e^{-\frac{(s-\mu)^2}{2\sigma^2}}.$$
 (19)

The asymptotic approximation (19) for P(s,B) is a normal distribution with mean  $\mu$  and variance  $\sigma^2$ . Since the particles are identical and independent, P(s,B) also represents the probability distribution of collision number for the particles. We note that the assumption that the particle collisions are independent holds only for large Stoke numbers. For small St, two particles that have recently collided would be more likely to collide with each other again, so that the collisions would no longer be independent.

The probability distribution function of the radial relative velocity (RRV) at contact is shown for different Stokes numbers in Figure 7. For large Stokes numbers (St > 10), the RRV distribution is found be closely skew-normal distribution, to fit by the  $y = \frac{5}{\sqrt{2\pi}} e^{-\frac{1}{2}(\frac{x-0.05}{0.2})^2} [1 + \text{erf}(\frac{24(x-0.05)}{\sqrt{2}})], \text{ where erf}(x) \text{ is the error function. For smaller values}$ of the Stokes numbers (e.g., St = 1.1), the RRV distribution is close to the exponential distribution,  $y = e^{2.4125-10.25x}$ . As St decreases, the mean value of the RRV distribution also decreases, implying small contact area and small amounts of charge transfer during collisions.

In these computations, it was assumed that each particle is initially completely covered by available charge carriers, which the particles gradually lose by collisions with other particles until no available charge carriers remain. We define a particle as being 'involved in the electrification processes' if it has undergone at least one collision but still has some available charge carriers remaining. The ratio of available charge carriers at the current time to that at the start of the computation is called the *charge carrier depletion ratio*,  $R_{H,n}(t)$ , which is defined for particle n by

$$R_{H,n}(t) = \frac{N_{H,n}(t)}{N_{H,n}(0)},\tag{20}$$

where  $N_{H,n}(0)$  and  $N_{H,n}(t)$  are the number of available charge carriers of particle n at the initial time and at time t, respectively. The charge carrier depletion ratio  $R_{H,n}(t)$  is equal to unity at the start of the computation for all particles, and it approaches zero at long time as all available charge carriers are expended by transferring onto colliding particles. Figure 8 shows the time development of the distribution of  $R_{H,n}(t)$  for all particles involved in the electrification process for different values of the total number of collisions B, for a case with St = 33.6. As the total collision number B increases, the peak of distribution moves from nearly unity to nearly zero.

A plot showing the p.d.f. of the charge carrier depletion ratio for different Stokes numbers when B=500,000 is given in Figure 9. At this intermediate stage, most of the particles are involved in the electrification process and the p.d.f. is observed to be close to a normal distribution. The mean value of the  $R_{H,n}(t)$  distribution represents the average ratio of charge carriers that have been expended at a given time. The distributions of  $R_{H,n}(t)$  are almost the same for cases with different Stokes numbers for large values of St, while the mean value of  $R_{H,n}(t)$  is larger for small St values. The p.d.f. distribution for  $R_{H,n}(t)$  at the midpoint of the electrification process, when the mean value  $\langle R_{H,n} \rangle \cong 0.5$ , is plotted in Figure 10 for different Stokes numbers. We similarly see that the normal distribution is a good fit for all cases, but that the variance of the distribution is somewhat smaller at small St than at large St values, which is related to the observed lower values of the relative radial velocity for small Stokes numbers.

The net charge on each particle is zero at the beginning of the computation. Charge is exchanged between the particles during the contact electrification process until the equilibrium state is reached, at which time all of the available charge carriers have been expended and after which the charge on each particle remains constant. A plot of the distribution of particle charge,  $q_p$ , in the equilibrium state is given in Figure 11. The equilibrium charge distribution is observed to form a nearly normal distribution which has somewhat smaller variance for small Stokes numbers, but to asymptote to a common curve for large Stokes numbers.

# 3.3. Contact electrification with bidisperse particle size and initial charge carrier density

The effect of different initial charge carrier densities was examined by setting half of the particles (Set A) to have double the initial charge carrier density as the other half of the particles (Set B), in a computation with St = 11.2. Since the particles in Set A with higher initial charge carrier density have more charge carriers available to lose in collisions than do the particles in Set B, we expect the particles in Set A to develop a net positive charge during the computation and the particles in Set B to correspondingly develop a net negative charge, where we assume that the charge carrier charge is negative. The net charge of all particles in a given set is denoted by Q, such that Q(A) is the net charge of particles in Set A and Q(B) is the net charge of particles in Set B. The value of Q for each set is plotted in Figure 12 as a function of time, showing the expected positive net charge development for particles in Set A and negative net charge development for particles in Set B. When all the available charge carriers have been expended, the system approaches an equilibrium state. The charge distribution in the equilibrium state is shown in Figure 13 for both sets of particles individually. While the charge distribution is

observed in the runs with identical charge carrier densities in Figure 11. The mean particle charge is equal with opposite sign for the two distributions, and the mean of the distributions is the same.

The effect of different particle sizes was examined using a bidisperse distribution in which half of the particles (Set C) are assigned a diameter of 1.25d and the other half of the particles (Set D) are assigned a diameter of 0.8d, where d is the particle diameter used in the computations in Section 3.2. The overall particle collision rate increases by 10% for the bidisperse distribution compared to computations with identical particle size. The p.d.f. distributions for different types of particles collisions are given in Figure 14. There are three types of collisions: collisions between two small particles, collisions between two large particles, and collisions between a large particle and a small particle. These three types of collisions are all observed to exhibit normal distributions. The distribution for collisions between two large particles has a larger mean value and a higher variance than does the distribution for collisions between two small particles, which is expected from the fact that the larger particles occupy a larger volume of the flow field than do the smaller particles. The distribution for collisions between large and small particles has a mean value and variance that are intermediate between the values for small-small collisions and that for large-large collisions. Also plotted in Figure 14 are the distribution for all collisions of the small particles and the distribution for all collisions of the large particles. If X is a random variable for a collision of a particle with another particle of the same size and Y is a random variable for a collision between particles of different sizes, then the total collision distribution for a given particle set has a mean  $\mu_{X+Y}$  and variance  $\sigma_{X+Y}$  that satisfy

$$\mu_{X+Y} = \mu_X + \mu_Y, \qquad \sigma_{X+Y}^2 = \sigma_X^2 + \sigma_Y^2 + 2\rho\sigma_X\sigma_Y,$$
 (21)

where the correlation parameter  $\rho$  vanishes when variables X and Y are independent. Based on the best-fit distributions for the total collisions of the large and small particles obtained in Figure 14, we find that  $\rho \approx 0.2$  for both the small and large particle sets. This result implies a non-zero correlation for collisions between particles of different sizes.

Since large particles have a larger number of available charge carriers than do small particles, the large particles on average give away more charge carriers than do the small particles over the course of the computation. This leads to a tendency for the larger particles to become positively charged and the smaller particles to be come negatively charged. A plot of the time variation of the total charge for all particles from the larger-size Set C and the smaller-size Set D is given in Figure 15a. Unlike the previous cases examined, the value of Q achieves a maximum (or minimum) value at a finite time for this case, after which the absolute value of Q decreases. This extremum value occurs because the collision rate for the large particles is more rapid than that for the small particles, since at high Stokes number the collision kernel varies in proportion to particle diameter squared (Abrahamson, 1975). As a consequence, the charge exchange from different types of collisions occurs over different time scales. The charge distribution for the large and small particles is shown in Figure 15b at time t = 130, at which B = 2,000,000. Both distributions have approximately normal form, with the mean value for the large particles slightly positive and that for the small particles slightly negative. The standard deviation for these distributions is significantly smaller for the small particles than it is for the large particles, and for both sets of particles the standard deviation is much larger than the mean value.

When both the particle size and the initial charge carrier density are different for the two particle sets, the results are a combination of those observed when each effect is examined independently. For instance, a computation was conducted in which half the particles (Set E) have diameter 1.25d with twice the initial charge carrier density as the other half (Set F) of the particles, which had smaller diameter 0.8d. A plot showing the time variation of the total charge Q for both sets of particles is given in Figure 16a, and the charge distribution is shown in Figure 16b. As in Figure 13, the mean values of the two sets of particles are significantly different, with the particles in Set E having a larger mean value than the particles in Set F. As in Figure 15b, the variance for the two sets of particles are also different, with the variance for the particles in Set E (the larger particles) being larger, and the peak value smaller, than for the particles in Set E (the smaller particles).

We note that while both differences in initial charge carrier density and in particle size can lead to a mean charge difference between the two sets of particles, the former effect is a lot stronger than the latter. For instance, in Figure 17 we plot results of a computation where half the particles (Set H) have diameter 1.25d and the other half (Set G) have diameter 0.8d. However, in this computation the smaller particles (Set G) were assigned a 10% larger initial charge carrier density than the large particles (Set H). The plot of the time variation of mean charge of each of these sets (Figure 17a) clearly indicates that the small particles become positively charged while the large particles become negatively charged, in contrast to the results observed in Figure 16a. However, the variance of the charge distribution for the small particles continues to be smaller than that of the large particles (Figure 17b), which has been consistently observed for all cases examined. Since the initial charge carrier density is largely determined by the material properties of the material, the observed strong sensitivity of the computed charge to this parameter is

consistent with historical identification of the direction of charge transfer in contact electrification in terms of material properties (via a triboelectric series).

#### 4. Conclusions

We have coupled a probabilistic version of a phenomenological contact electrification model to a pseudo-spectral direct numerical simulation method for homogeneous turbulence and a hard-sphere discrete-element method for particle transport and collisions in order to advance understanding of the effect of fluid turbulence on particle contact electrification. The observed distributions of particle charge development are found to be insensitive to Stokes number for St greater than about 6, but to be highly sensitive to Stokes number for values of St near unity.

The probability density functions for number of collisions and for number of charge carriers are observed to be approximately normally distributed for high St cases, as would be expected from the central limit theorem for independent random processes. However, for small St cases (near unity and below), the particle relative radial velocity at collision is observed to approach an exponential distribution, indicating an increased tendency for collision between neighboring particles, which leads to a break-down of the assumption of independent collisions. The particle charge approaches a constant value at large time, when all of the available charge carriers have been removed from the particle surfaces via collisions. The resulting charge distribution is found to be well approximated by a normal distribution for all Stokes number values examined. Cases with high Stokes number (above about 6) approach an asymptotic charge distribution which is nearly independent of Stokes number. Cases with lower Stokes number values, near unity, also seem to approach a nearly normal charge distribution, but with significantly smaller variance than for the high Stokes number cases.

Simulations in which half of the particles had a higher initial value of the charge carrier density than the other half of the particles caused a strong shift in the charge distributions without change in shape, in the direction of positive charge for the particles with higher initial charge carrier density and in the direction of negative charge for the other half of the particles. Simulations in which half of the particles were larger than the other half of the particles caused the charge distribution for the larger particles to have larger variance and smaller peak than that for the smaller particles, due to the higher collision rate of the larger particles. These two trends were found to be preserved in an additive fashion for simulations with differences in both particle size and initial charge carrier density.

# Acknowledgments

We gratefully acknowledge support of this work from the U.S. National Science Foundation [grant number CBET-1332472].

#### References

Abrahamson, J., Collision rates of small particles in a vigorously turbulent fluid. *Chemical Engineering Science* **30**, 1371-1379 (1975).

Apodaca, M.M., Wesson, P.J., Bishop, K.J.M., Ratner, M.A., and Grzybowski, B.A., Contact electrification between identical materials. *Angewandte Chemie International Edition* **49**, 946-949 (2010).

Baytekin, H.T., Patashinski, A.Z., Branicki, M., Baytekin, B., Soh, S., and Grzybowski, B.A., The mosaic of surface charge in contact electrification. *Science* **333**, 308-312 (2011).

Baytekin, H.T., Baytekin, B., Incorvati, J.T., and Grzybowski, B.A., Material transfer and polarity reversal in contact charging. *Angewandte Chemie International Edition* **124**, 4927-4931 (2012).

Bec, J., Biferale, L., Cencini, M., Lanotte, A., Musacchio, S., Toschi, F., Heavy particle concentration in turbulence at dissipative and inertial scales. *Physical Review Letters* **98**, 084502 (2007).

Beck, C., Superstatistics: Theoretical concepts and physical applications. In *Anomalous Transport: Foundations and Applications*, edited by R. Klages, G. Radons and I. M. Sokolov, Wiley-VCH Verlag GmbH & Co. KGaA, Weinheim, Germany (2008).

Biferale L, Boffetta G, Celani A, Devenish BJ, Lanotte A, Toschi F, Multifractal statistics of Lagrangian velocity and acceleration in turbulence. *Physical Review Letters* **93**(6), 064502 (2004).

Brook, M., Moore, C.B. and Sigurgeirsson, T., Lightning in volcanic clouds. *Journal of Geophysical Research* **79**, 472-475 (1974).

Castle, G.S.P., Contact charging between particles: some current understanding. Proceedings Electrostatics Society of America Annual Meeting, Paper M1 (2008).

Crowe, C.T., Schwarzkopf, J.D., Sommerfeld, M., Tsuji, Y., *Multiphase Flows with Droplets and Particles*, 2nd ed., CRC Press, Boca Raton, Florida (2011).

Desch, S.J., Cuzzi, J.N., The generation of lightning in the solar nebula. *Icarus* **143**, 87-105 (2000).

Dizaji, F.F., and Marshall, J.S., An accelerated stochastic vortex structure method for particle collision and agglomeration in homogeneous turbulence. *Physics of Fluids* **28**, 113301 (2016).

Duff, N. and Lacks, D.J., Particle dynamics simulations of triboelectric charging in granular insulator systems. *Journal of Electrostatics* **66**, 51-57 (2008).

Eckhoff, R.K., *Dust Explosions in the Process Industries*, 2nd ed. Butterworth-Heinemann, Oxford, U.K. (1997).

Eden, H.F. and Vonnegut, B., Electrical breakdown caused by dust motion in low-pressure atmospheres: Considerations for Mars. *Science* **180**, 962-963 (1973).

Falkovich, G., Pumir, A., Intermittent distribution of heavy particles in a turbulent flow. *Physics of Fluids* **16**(7), L47-L50 (2004).

Fayed, H.E., and Ragab, S.A., Direct numerical simulation of particles-bubbles collisions kernel in homogeneous isotropic turbulence. *Journal of Computational Multiphase Flows* **5**(3), 167-188 (2013).

Forward, K.M., Lacks, D.J. and Sankaran, R.M., Particle-size dependent bipolar charging of Martian regolith simulant. *Geophysical Research Letters* **36**, L13201 (2009).

Grits, B., Pinsky, M., Khain, A., Investigation of small-scale droplet concentration inhomogeneities in a turbulent flow. *Meteorology and Atmospheric Physics* **92**, 91-204 (2006).

Harper, W.R., Contact and Frictional Electrification. Oxford University Press, New York (1967).

Harrison, R.G., Barth, E., Esposito, F., Merrison, J., Montmessin, F., Aplin, K.L., Borlina, C., Berthelier, J.J., Déprez, G., Farrell, W.M., Houghton, I.M.P., Renno, N.O., Nicoll, K.A., Tripathi, S.N., and Zimmerman, M., Applications of electrified dust and dust devil electrodynamics to Martian atmospheric electricity. *Space Science Reviews* (in press, 2016).

Hartquist, T.W., Havnes, O. and Morfill, G.E., The effects of charged dust on Saturn's rings. *Astronomy & Geophysics* **44**(5), 26-30 (2003).

Helsdon, J.H., Wojcik, W.A., and Farley, R.D., An examination of thunderstorm-charging mechanisms using two-dimensional storm electrification model. *Journal of Geophysical Research* **106**(D1), 1165-1192 (2001).

Hertz, H., Über die Berührung fester elastischer Körper. *J. reine und angewandte Mathematik* **92**, 156-171 (1882).

Kempf, S., Beckmann, U., Srama, R., Horanyi, M., Auer, S., and Grün, E., The electrostatic potential of E ring particles. *Planetary and Space Science* **54**, 999-1006 (2006).

Kittaka, S., and Murata, Y., Photoelectric emission and contact charging of vacuum-UV irradiated polymers. *Japanese Journal of Applied Physics* **18**(3), 515-521 (1979).

Kok, J.F., and Lacks, D.J., Electrification of granular systems of identical insulators. *Physical Review E* **79**, 051304 (2009).

Lacks, D.J., and Levandovsky, A., Effect of particle size distribution on the polarity of triboelectric charging in granular insulator systems. *Journal of Electrostatics* **65**,107-112 (2007).

Lacks, D.J., and Sankaran, R.M., Contact electrification of insulating materials. *Journal of Physics D: Applied Physics* **44**, 453001 (2011).

La Porta, A., Voth, G.A., Crawford, A.M., Alexander, J., and Bodenschatz, E., Fluid particle acceleration in fully developed turbulence. *Nature* **409**, 1017-1019 (2001).

Latham, J. The electrification of snowstorms and sandstorms. *Quarterly Journal of the Royal Meteorological Society* **90**, 91-95 (1964).

Lowell, J., and Rose-Innes, A.C., Contact electrification. *Advances in Physics* **29**(6), 947-1023 (1980).

Lowell, J., and Truscott, W.S., Triboelectrification of identical insulators: II. Theory and further experiments. *Journal of Physics D: Applied Physics* **19**, 1281-1298 (1986).

Lundgren, T.S., Linearly forced isotropic turbulence. *Annual Research Briefs*, pp. 461-473, CTR, Stanford (2003).

Marshall, J.S. and Li, S., *Adhesive Particle Flow: A Discrete Element Approach*, Cambridge University Press, New York (2014).

McCarty, L.S. and Whitesides, G.M., Electrostatic charging due to separation of ions at interfaces: contact electrification of ionic electrets. *Angewandte Chemie International Edition* **47**, 2188-2207 (2008).

Monaghan, J.J., Extrapolating B splines for interpolation. *Journal of Computational Physics* **60**, 253-262 (1985).

Mordant, N., Lévêque, E., and Pinton, J.F., Experimental and numerical study of the Lagrangian dynamics of high Reynolds turbulence. *New Journal of Physics* **6**, 116 (2004).

Pähtz, T., Herrmann, H.J., and Shinbrot, T., Why do particle clouds generate electric charges? *Nature Physics* **6**(5), 364-368 (2010).

Reynolds AM, Superstatistical mechanics of tracer-particle motions in turbulence. *Physical Review Letters* **91**(8), 084503 (2003).

Rosales, C., and Meneveau, C., Linear forcing in numerical simulations of isotropic turbulence: physical space implementations and convergence properties. *Physics of Fluids* **17**(9), 095106 (2005).

Saffman, P.G., The lift on a small sphere in a slow shear flow. *Journal of Fluid Mechanics* **22**, 385-400 (1965).

Saffman, P.G., Corrigendum to 'The lift force on a small sphere in a slow shear flow'. *Journal of Fluid Mechanics* **31**, 624 (1968).

Saffman, P.G. and Turner, J.S., On the collision of drops in turbulent clouds. *Journal of Fluid Mechanics* **1**(1), 16-30 (1956).

Saunders, C.P.R., Thunderstorm electrification laboratory experiments and charging mechanisms. *Journal of Geophysical Research* **99**(D5), 10773-10779 (1994).

Siu, T., Cotton, J., Mattson, G., and Shinbrot, T., Self-sustaining charging of identical colliding particles. *Physical Review E* **89**, 052208 (2014).

Squires, K.D., Eaton, J.K., Preferential concentration of particles by turbulence. *Physics of Fluids A* **3**, 1169-1178 (1991).

Sundaram, S., and Collins, L.R., Numerical considerations in simulating a turbulent suspension of finite-volume particles. *Journal of Computational Physics* **124**, 337-350 (1996).

Sundaram, S. and Collins, L.R., Collision statistics in an isotropic particle-laden turbulent suspension. I. Direct numerical simulations. *Journal of Fluid Mechanics* **335**, 75-109 (1997).

Tomas, R. J. et al. Electrical activity during the 2006 Mount St Augustine volcanic eruptions. *Science* **315**, 1097 (2007).

Vincent, A., and Meneguzzi, M., The spatial structure and statistical properties of homogeneous turbulence. *Journal of Fluid Mechanics* **225**, 1-20 (1991).

Voth, G.A., Satyanarayan, K., and Bodenschatz, E., Lagrangian acceleration measurements at large Reynolds numbers. *Physics of Fluids* **10**(9), 2268-2280 (1998).

Waitukaitis, S.R., Lee, V., Pierson, J.M., Forman, S.L., and Jaeger, H.M., Size-dependent same-material tribocharging in insulating grains. *Physical Review Letters* **112**, 218011 (2014).

Wang, L.-P., Wexler, A.S., and Zhou, Y., Statistical mechanical description and modeling of turbulent collision of inertial particles. *Journal of Fluid Mechanics* **415**, 117–153 (2000).

Williams, M.W., Triboelectric charging of insulators – mass transfer versus electrons/ions. *Journal of Electrostatics* **70**, 233-234 (2012).

Williams, E., Nathou, N., Hicks, E., Pontikis, C., Russell, B., Miller, M. and Bartholomew, M.J., The electrification of dust-lofting gust fronts ('haboobs') in the Sahel. *Atmospheric Research* **91**, 292-298 (2009).

Xie, L., Li, G., Bao, N., and Zhou, J., Contact electrification by collision of homogenous particles. *Journal of Applied Physics* **113**, 184908 (2013).

Zheng, X.J., Electrification of wind-blown sand: Recent advances and key issues. *European Physics Journal E* **36**, 138 (2013)

# **Figure Captions**

- Figure 1. Plots characterizing direct numerical simulations of turbulent flow: (a) power spectrum showing  $k^{-5/3}$  scaling in inertial range, (b) velocity probability density function with DNS data (symbols) and best-fit Gaussian curve (solid line), and (c) probability density function for acceleration with DNS data (symbols) and best-fit function to the experimental data of La Porta et al. (2001) (solid line).
- Figure 2. The collision rate per unit volume,  $\dot{n}_c$ , for different values of the Kolmogorov-scale Stokes number St.
- Figure 3. Comparison of dimensionless collision rate,  $\dot{n}_c / (\pi d^2 n_p^2 u_0)$ , to values obtained by other investigators as a function of Stokes number. The plots show DNS data of Sundaram and Collins (1997) for  $Re_{\lambda} = 54$  (squares, blue line), DNS data of Wang *et al.* (2000) for  $Re_{\lambda} = 75$  (circles, red line), DNS data of Fayed and Ragab (2013) for  $Re_{\lambda} = 96$  (deltas, green line), and our DNS result for  $Re_{\lambda} = 99$  (×'s, black line).
- Figure 4. The time development of total transferred charge  $Q_{trans}$  for different Stokes numbers.
- Figure 5. The probability density function (p.d.f.) of the number of collisions for a particle,  $b_p$ , for a case with St = 33.6, plotted at different values of the total number of collisions in the system, B. The black solid lines represent best-fit normal distributions.
- Figure 6. The probability density function (p.d.f.) of nondimensionless collision number of particle,  $b_p/B$ , for different Stokes numbers when the total number of collisions B = 500,000. The black solid line represents the best-fit normal distribution in the high-St limit.
- Figure 7. The probability density function (p.d.f.) of radial relative velocity at contact,  $w_r$ , for different Stokes numbers when B = 500,000. The solid line is a skew-normal distribution, and the dashed line is an exponential distribution.
- Figure 8. Time variation of the p.d.f. of the charge carrier depletion ratio  $R_{H,n}(t)$  for particles involved in the electrification process for a case with St = 33.6, plotted at different values of the total number of collisions B.
- Figure 9. The probability density function (p.d.f.) of the charge carrier depletion ratio  $R_H$  for different Stokes numbers when the total number of collisions B = 500,000. The solid line denotes the best-fit normal distribution to the high St cases.
- Figure 10. The distribution of  $R_H$  for different Stokes numbers when the mean value  $\langle R_{H,n} \rangle \cong 0.5$ . The solid line is the best-fit Gaussian to the high St cases.

- Figure 11. The distribution of charge of particle  $q_p$  for different Stokes numbers when B = 2,000,000. The solid line is the best-fit Gaussian curve to the high St cases.
- Figure 12. The time development of total charge Q for same-size particles with half the particles (red line A) assigned twice the initial charge carrier density as the other half of the particles (blue line B).
- Figure 13. Charge distribution  $q_p$  for particles shown in Figure 12 at the equilibrium time, where results for particles with high initial charge carrier density (red line A, circles) and particles with low initial charge carrier density (blue line B, gradients) are plotted separately. The solid lines represent best-fit normal distributions and the dashed lines point out the mean particle charge in each set.
- Figure 14. The probability density function (p.d.f.) of the number of collisions for a particle,  $b_p$ , for different types of collisions when B=2,000,000. The collision types include small-small particle collision (SS), large-large particle collision (LL), and small-large particle collision (SL). The SS+SL data represents all the collisions for small particles, and the LL+SL data represents all collisions for the large particles. The solid and dashed lines represent best-fit normal distributions.
- Figure 15. Results for a run with different size particles and the same initial charge carrier density: (a) time development of total charge Q and (b) charge distribution for large particles (red line C, circles) and small particles (blue line D, gradients) at time t = 130, corresponding to B = 2,000,000. Mean values are indicated by dashed lines in (b).
- Figure 16. Results for a run with different size particles, in which the large particles have higher initial charge carrier density than do the small particles: (a) time development of total charge Q and (b) charge distribution at the end of the computation for large particles (red line E, circles) and small particles (blue line F, gradients). Mean values are indicated by dashed lines in (b).
- Figure 17. Results for a run with different size particles, in which the small particles have 10% higher initial charge carrier density than do the large particles: (a) time development of total charge Q and (b) charge distribution at the end of the computation for large particles (red line H, circles) and small particles (blue line G, gradients). Mean values are indicated by dashed lines in (b).

Table 1. Dimensionless simulation parameters and physical parameters of the fluid turbulence.

Simulation Parameters		<b>Turbulence Parameters</b>	
Time step	0.005	Turbulent kinetic energy, q	0.115
Cycles	50,000	Dissipation rate, $\varepsilon$	0.009
Grid	128 <sup>3</sup>	Kinematic viscosity, <i>v</i>	0.001
		Integral length, $\ell_0$	1.18
		Taylor microscale, $\lambda$	0.357
		Kolmogorov length, $\eta$	0.0183
		Integral velocity, $u_0$	0.277
		Integral time, $T_{\ell}$	4.26

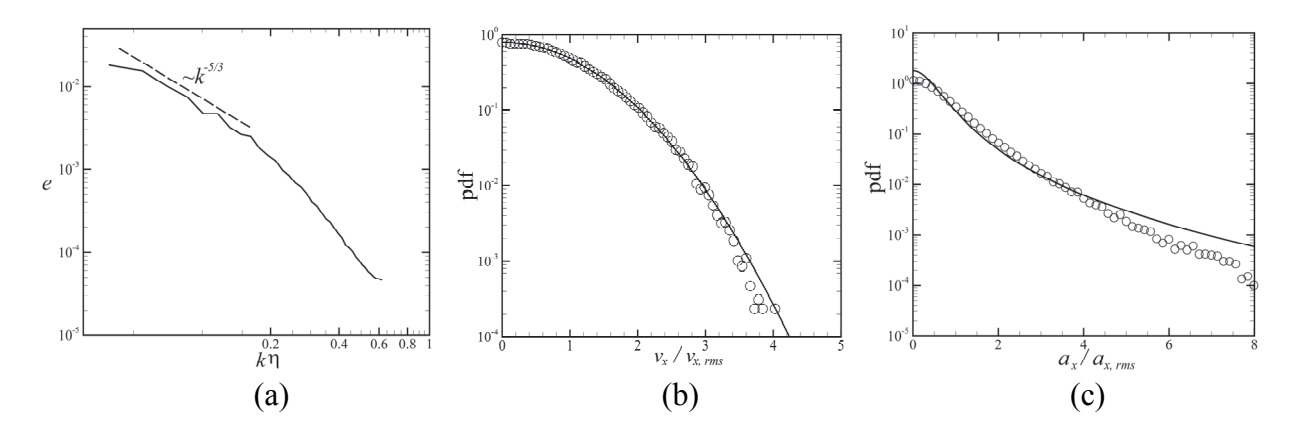


Figure 1. Plots characterizing direct numerical simulations of turbulent flow: (a) power spectrum showing  $k^{-5/3}$  scaling in inertial range, (b) velocity probability density function with DNS data (symbols) and best-fit Gaussian curve (solid line), and (c) probability density function for acceleration with DNS data (symbols) and best-fit function to the experimental data of La Porta et al. (2001) (solid line).

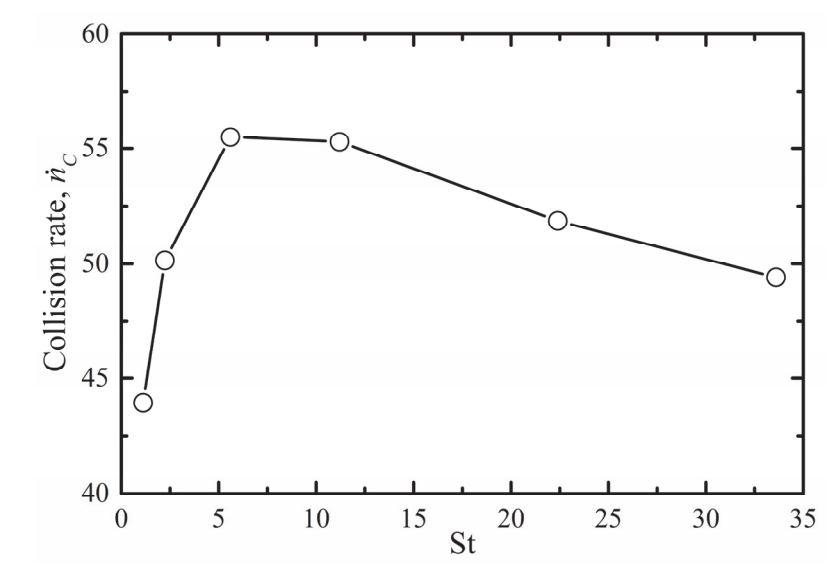


Figure 2. The collision rate per unit volume,  $\dot{n}_c$ , for different values of the Kolmogorov-scale Stokes number St.

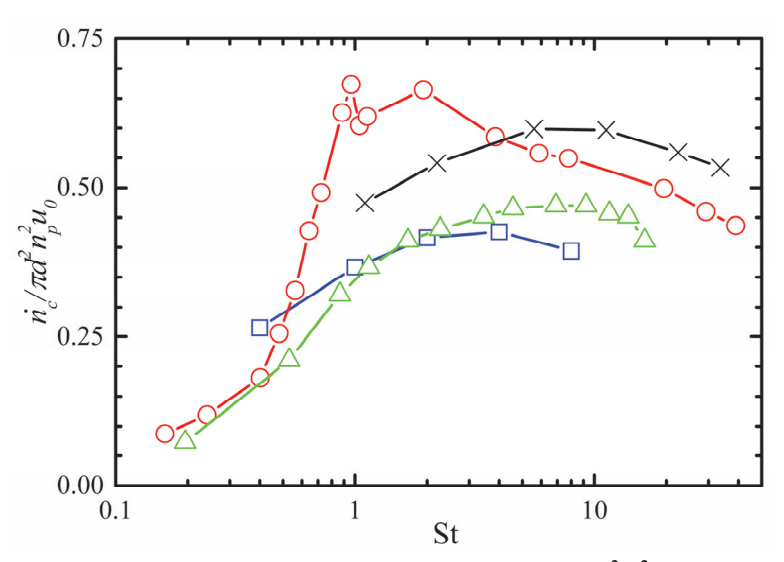


Figure 3. Comparison of dimensionless collision rate,  $\dot{n}_c / (\pi d^2 n_p^2 u_0)$ , to values obtained by other investigators as a function of Stokes number. The plots show DNS data of Sundaram and Collins (1997) for  $Re_{\lambda} = 54$  (squares, blue line), DNS data of Wang *et al.* (2000) for  $Re_{\lambda} = 75$  (circles, red line), DNS data of Fayed and Ragab (2013) for  $Re_{\lambda} = 96$  (deltas, green line), and our DNS result for  $Re_{\lambda} = 99$  (×'s, black line).

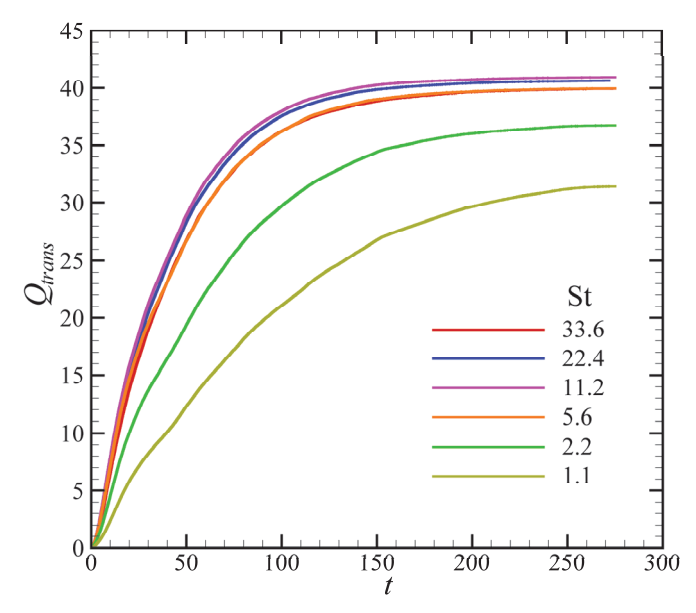


Figure 4. The time development of total transferred charge  $Q_{trans}$  for different Stokes numbers.

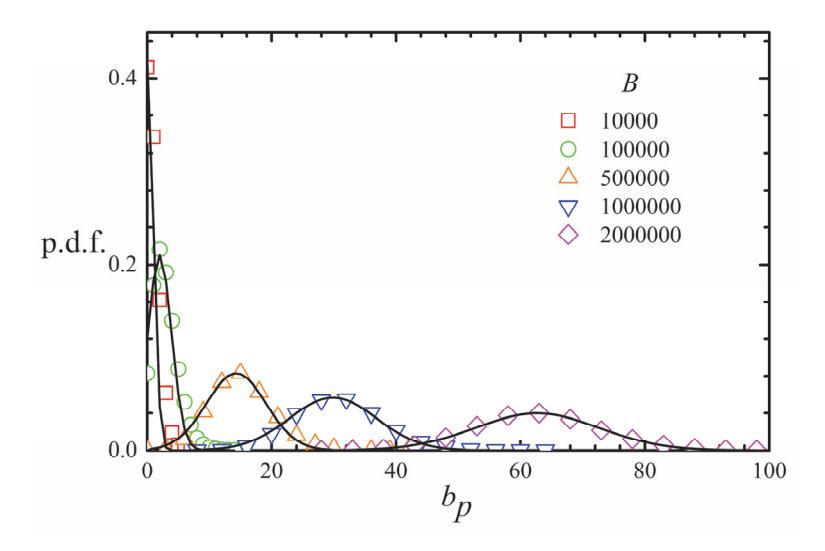


Figure 5. The probability density function (p.d.f.) of the number of collisions for a particle,  $b_p$ , for a case with St = 33.6, plotted at different values of the total number of collisions in the system, B. The black solid lines represent best-fit normal distributions.

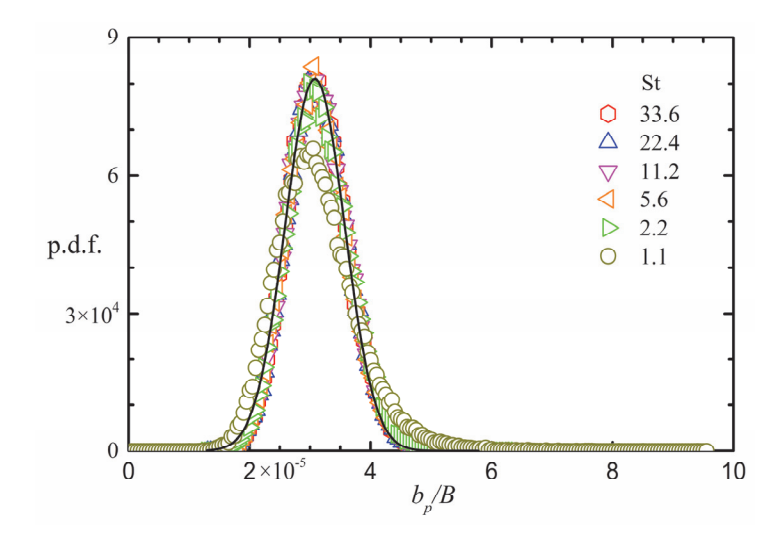


Figure 6. The probability density function (p.d.f.) of nondimensionless collision number of particle,  $b_p/B$ , for different Stokes numbers when the total number of collisions B = 500,000. The black solid line represents the best-fit normal distribution in the high-St limit.

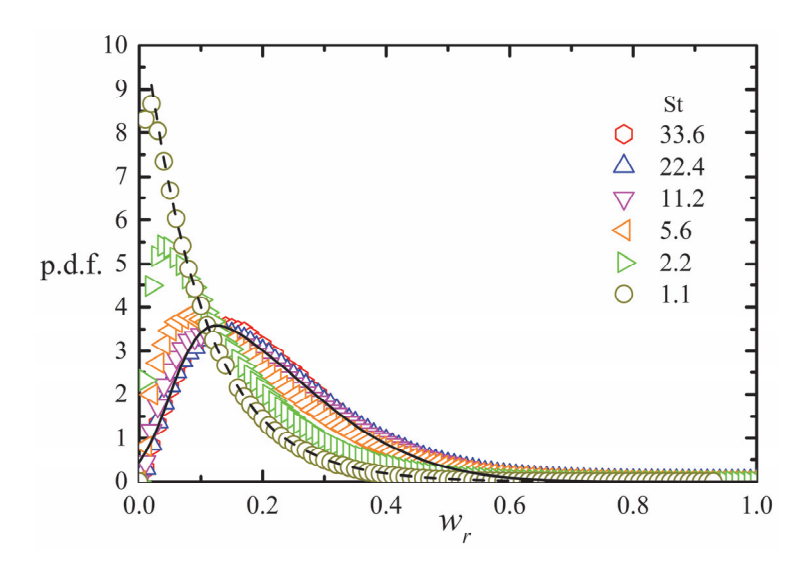


Figure 7. The probability density function (p.d.f.) of radial relative velocity at contact,  $w_r$ , for different Stokes numbers when B = 500,000. The solid line is a skew-normal distribution, and the dashed line is an exponential distribution.

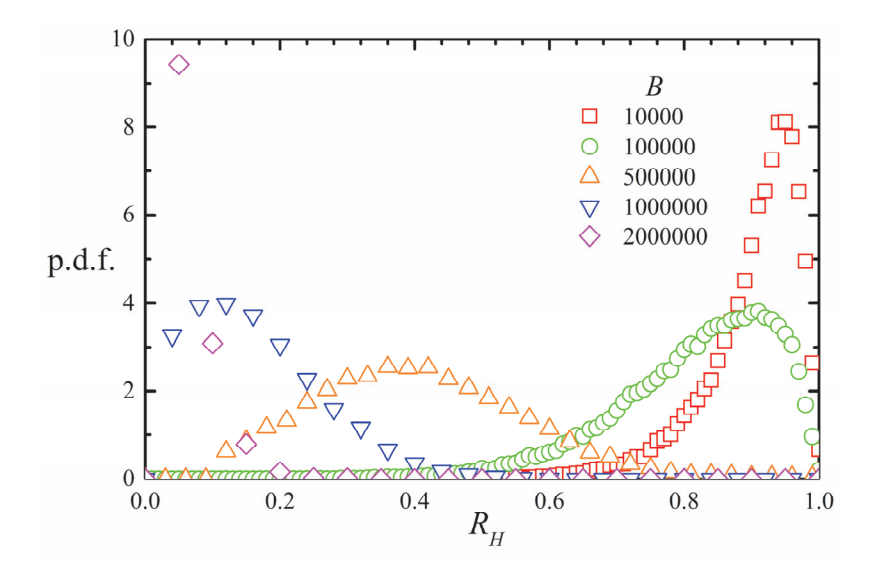


Figure 8. Time variation of the p.d.f. of the charge carrier depletion ratio  $R_{H,n}(t)$  for particles involved in the electrification process for a case with St = 33.6, plotted at different values of the total number of collisions B.

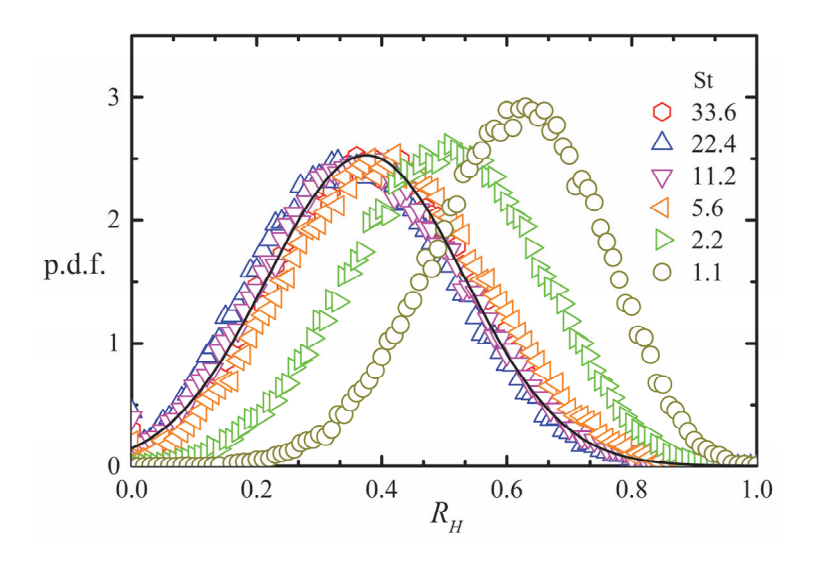


Figure 9. The probability density function (p.d.f.) of the charge carrier depletion ratio  $R_H$  for different Stokes numbers when the total number of collisions B = 500,000. The solid line denotes the best-fit normal distribution to the high St cases.

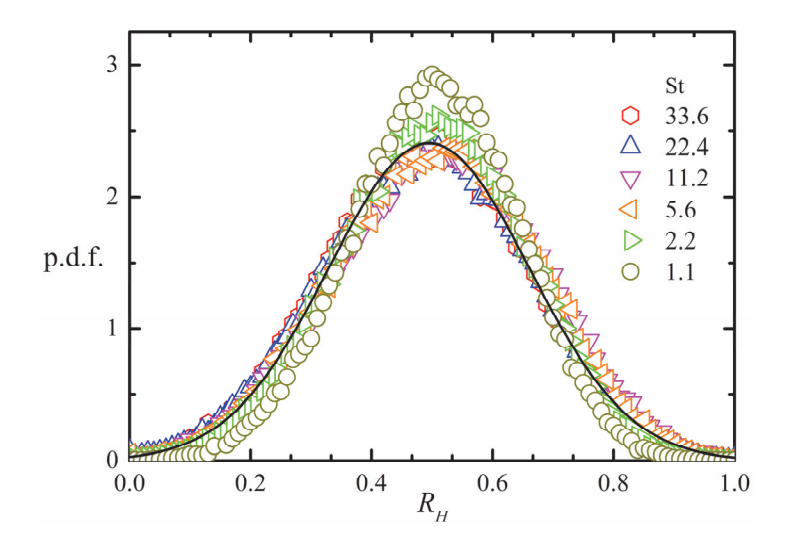


Figure 10. The distribution of  $R_H$  for different Stokes numbers when the mean value  $\langle R_{H,n} \rangle \cong 0.5$ . The solid line is the best-fit Gaussian to the high St cases.

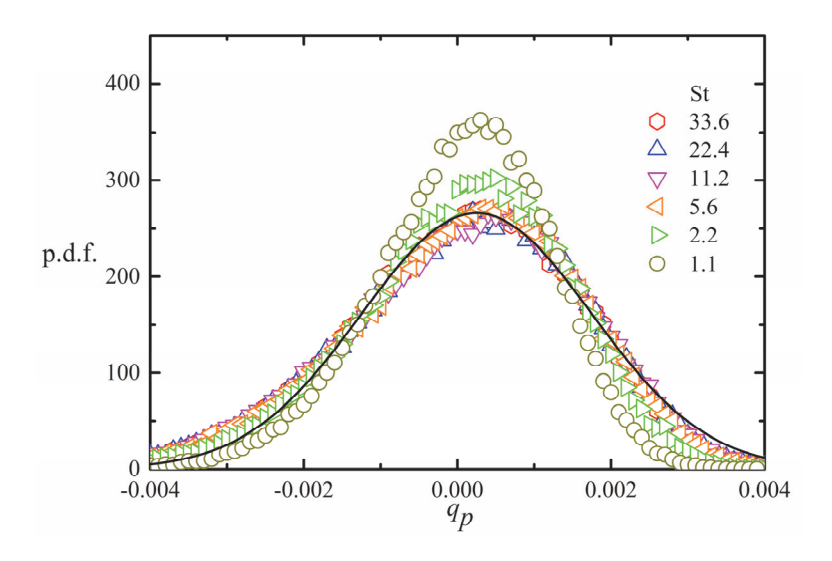


Figure 11. The distribution of charge of particle  $q_p$  for different Stokes numbers when B=2,000,000. The solid line is the best-fit Gaussian curve to the high St cases.

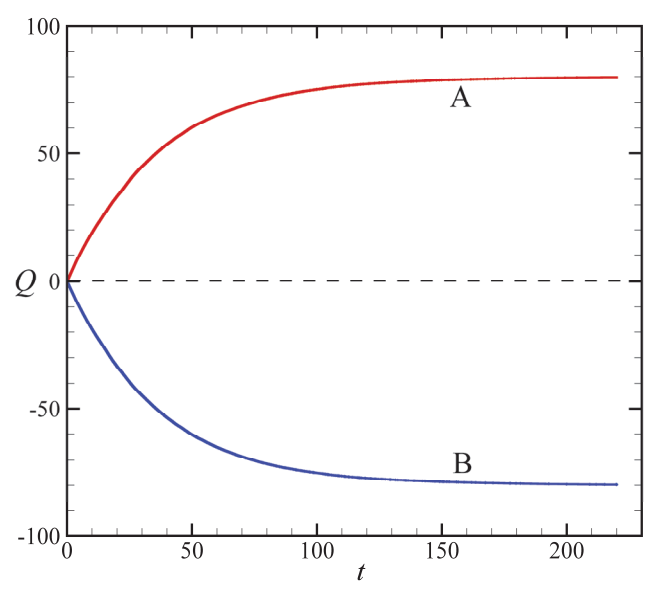


Figure 12. The time development of total charge Q for same-size particles with half the particles (red line A) assigned twice the initial charge carrier density as the other half of the particles (blue line B).

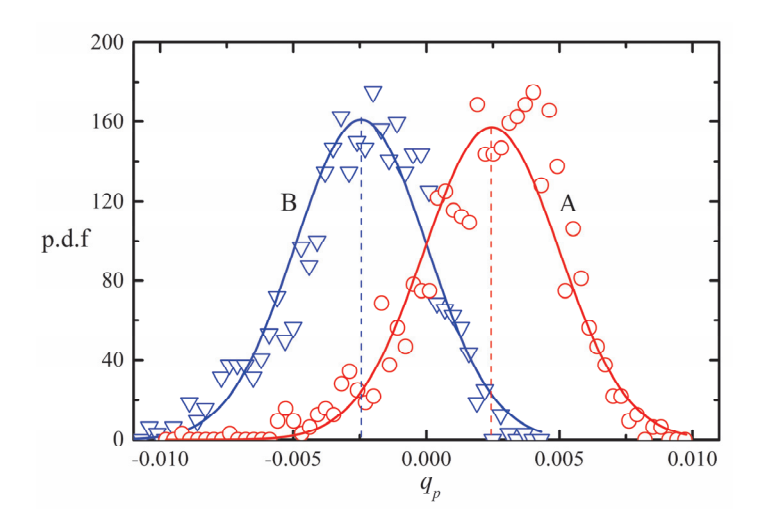


Figure 13. Charge distribution  $q_p$  for particles shown in Figure 12 at the equilibrium time, where results for particles with high initial charge carrier density (red line A, circles) and particles with low initial charge carrier density (blue line B, gradients) are plotted separately. The solid lines represent best-fit normal distributions and the dashed lines point out the mean particle charge in each set.

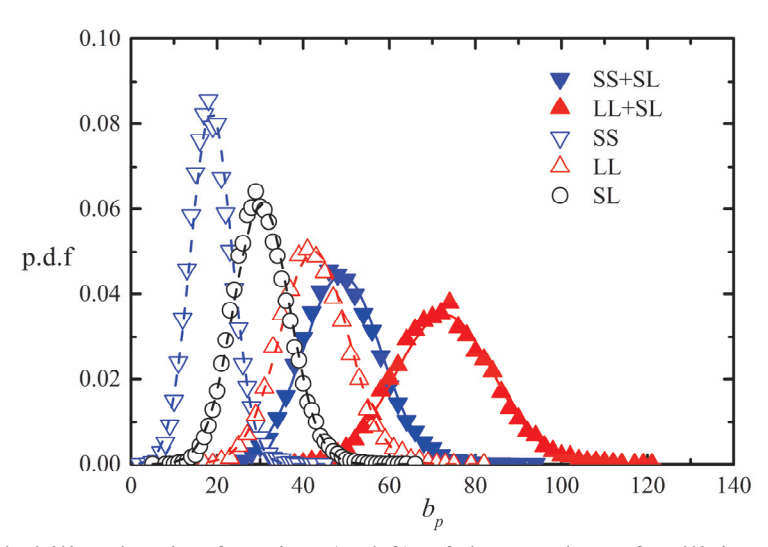


Figure 14. The probability density function (p.d.f.) of the number of collisions for a particle,  $b_p$ , for different types of collisions when B=2,000,000. The collision types include small-small particle collision (SS), large-large particle collision (LL), and small-large particle collision (SL). The SS+SL data represents all the collisions for small particles, and the LL+SL data represents all collisions for the large particles. The solid and dashed lines represent best-fit normal distributions.

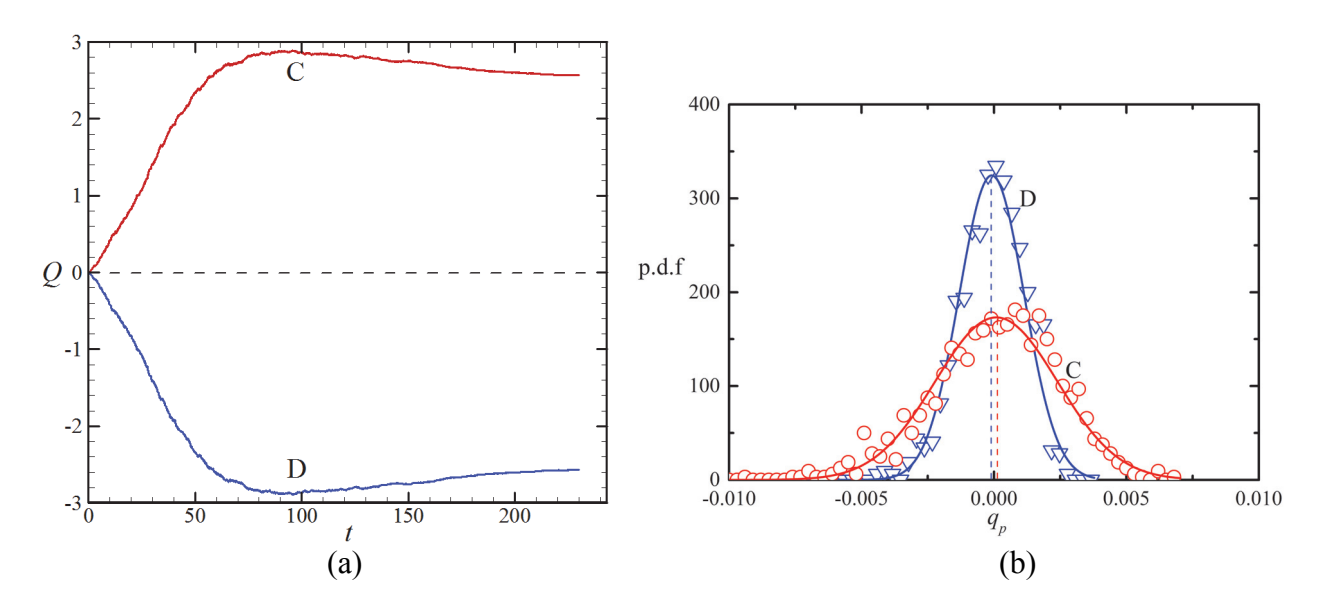


Figure 15. Results for a run with different size particles and the same initial charge carrier density: (a) time development of total charge Q and (b) charge distribution for large particles (red line C, circles) and small particles (blue line D, gradients) at time t = 130, corresponding to B = 2,000,000. Mean values are indicated by dashed lines in (b).

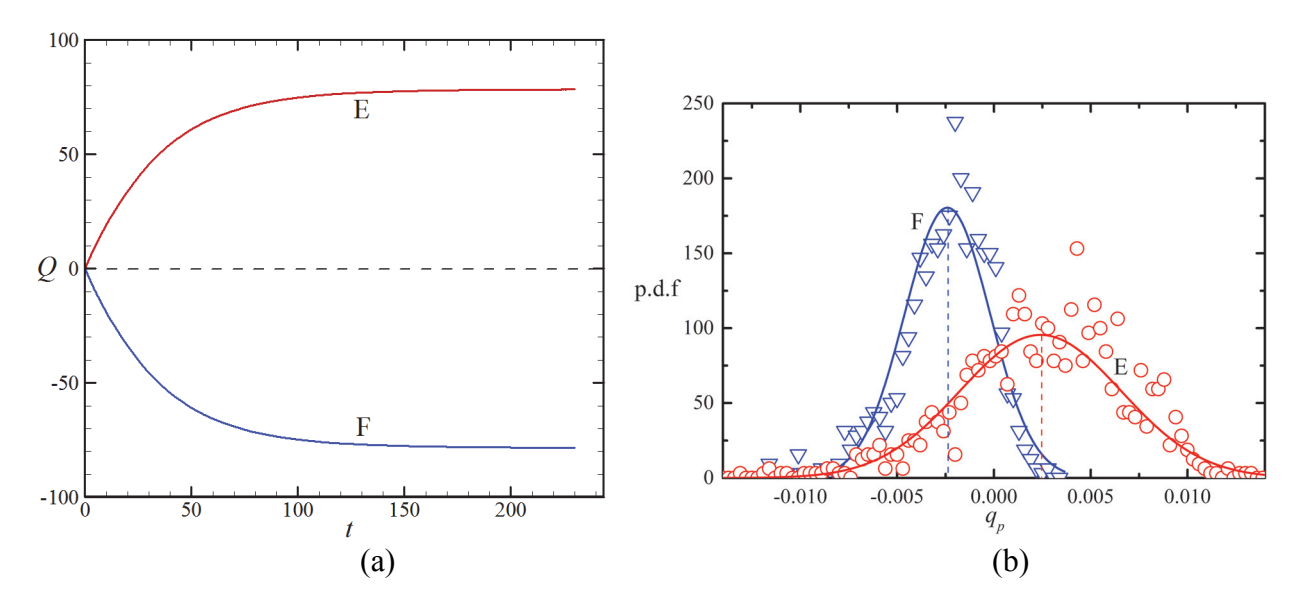


Figure 16. Results for a run with different size particles, in which the large particles have higher initial charge carrier density than do the small particles: (a) time development of total charge Q and (b) charge distribution at the end of the computation for large particles (red line E, circles) and small particles (blue line F, gradients). Mean values are indicated by dashed lines in (b).

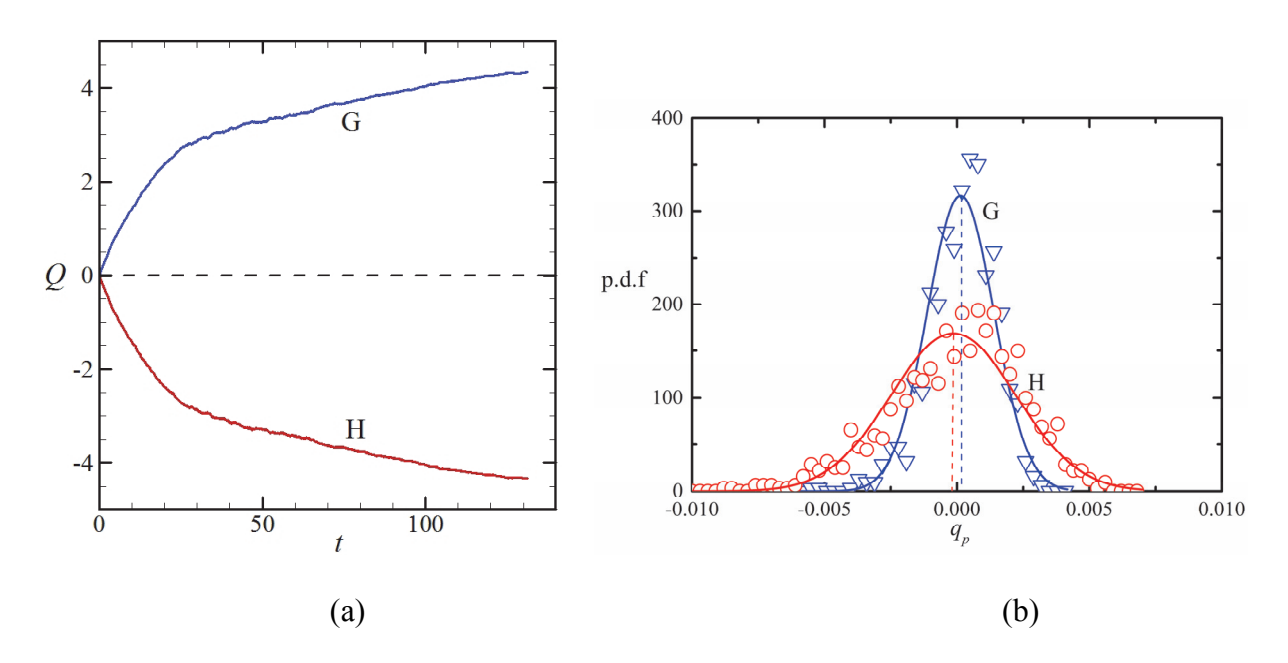


Figure 17. Results for a run with different size particles, in which the small particles have 10% higher initial charge carrier density than do the large particles: (a) time development of total charge Q and (b) charge distribution at the end of the computation for large particles (red line H, circles) and small particles (blue line G, gradients). Mean values are indicated by dashed lines in (b).